AGU PUBLICATIONS

JGR

Journal of Geophysical Research: Atmospheres

RESEARCH ARTICLE
10.1002/2015JD024238

Key Points:
- Extreme precipitation response to SST increase can be highly nonlinear
- Spatial variability of subgrid-scale vertical motions inadequately parametrized
- Convection-permitting models therefore needed to capture precipitation response

Supporting Information:
- Text S1 and Figures S1–S6

Correspondence to:
E. P. Meredith,
emeredith@geomar.de

Citation:
Meredith, E. P., D. Maraun, V. A. Semenov, and W. Park (2015), Evidence for added value of convection-permitting models for studying changes in extreme precipitation, *J. Geophys. Res. Atmos.*, *120*, 12,500–12,513, doi:10.1002/2015JD024238.

Received 18 SEP 2015
Accepted 2 DEC 2015
Accepted article online 11 DEC 2015
Published online 22 DEC 2015

Evidence for added value of convection-permitting models for studying changes in extreme precipitation

Edmund P. Meredith[1], Douglas Maraun[1,2], Vladimir A. Semenov[1,3,4,5], and Wonsun Park[1]

[1]GEOMAR Helmholtz Centre for Ocean Research Kiel, Kiel, Germany, [2]Wegener Center for Climate and Global Change, University of Graz, Graz, Austria, [3]A.M. Obukhov Institute of Atmospheric Physics, Russian Academy of Sciences, Moscow, Russia, [4]P.P. Shirshov Institute of Oceonology, Russian Academy of Sciences, Moscow, Russia, [5]Institute of Geography, Russian Academy of Sciences, Moscow, Russia

Abstract Climate model resolution can affect both the climate change signal and present-day representation of extreme precipitation. The need to parametrize convective processes raises questions about how well the response to warming of convective precipitation extremes is captured in such models. In particular, coastal precipitation extremes can be sensitive to sea surface temperature (SST) increase. Taking a recent coastal precipitation extreme as a showcase example, we explore the added value of convection-permitting models by comparing the response of the extreme precipitation to a wide range of SST forcings in an ensemble of regional climate model simulations using parametrized and explicit convection. Compared at the same spatial scale, we find that the increased local intensities of vertical motion and precipitation in the convection-permitting simulations play a crucial role in shaping a strongly nonlinear extreme precipitation response to SST increase, which is not evident when convection is parametrized. In the convection-permitting simulations, SST increase causes precipitation intensity to increase only until a threshold is reached, beyond which further SST increase does not enhance the precipitation. This flattened response results from an improved representation of convective downdrafts and near-surface cooling, which damp the further intensification of precipitation by stabilizing the lower troposphere locally and also create cold pools that cause subsequent convection to be triggered at sea, rather than by the coastal orography. These features are not well represented in the parametrized convection simulations, resulting in precipitation intensity having a much more linear response to increasing SSTs.

1. Introduction

Precipitation extremes can strongly affect society. Understanding the response of extreme precipitation to a changing climate and how this is represented in climate models is thus an important challenge. The intensity of precipitation extremes is expected to increase in a warming climate [*Allen and Ingram*, 2002; *Trenberth*, 1999]. Such an increase has been detected in observational studies [*Karl and Knight*, 1998; *Groisman et al.*, 2005; *Seneviratne et al.*, 2012; *Donat et al.*, 2013] and is also projected by global climate models [*Semenov and Bengtsson*, 2002; *Kharin et al.*, 2007; *Orlowsky and Seneviratne*, 2011], primarily in the tropics and high latitudes.

The representation of precipitation extremes in climate models, however, has been shown to be highly sensitive to model resolution, much more so than that of the mean [*Volosciuk et al.*, 2015]. Additionally, there is a growing body of evidence [*Kendon et al.*, 2012; *Chan et al.*, 2014a; *Ban et al.*, 2014] suggesting that convection-permitting resolution (O(~2 km)) is essential for accurately capturing midlatitude summertime convective extremes.

In achieving higher resolutions that more faithfully resolve extreme precipitation events, downscaling can add value to general circulation model (GCM) output. When considering the added value (AV) of higher resolutions, a distinction should be drawn between adding fine-scale detail and adding value at the spatial scale of the driving climate model. For precipitation, the potential AV of increased model resolution is greatest (i) at short temporal scales, (ii) during the warm season, i.e., when convection dominates, and (iii) in regions of complex topography, regardless of the season and temporal scale [*Di Luca et al.*, 2012]. Further AV (for multiple variables) is achieved in coastal zones and in environments with high mesoscale variability [*Feser et al.*, 2011]. Convection-permitting resolution yields additional AV through the improved representation of both the diurnal convective cycle and deep convective processes [*Hohenegger et al.*, 2008; *Prein et al.*, 2013].

Importantly, AV not only refers to the representation of present-day climate but in particular to the representation of the corresponding climate change signal. GCM resolution, for example, is known to influence the

strength of the response to warming of precipitation extremes [*Kitoh et al*., 2009; *Li et al*., 2011b; *Yang et al*., 2014]. Additionally, convection-permitting resolution is most likely essential to correctly capture the climate change signal of summertime convective extremes [*Kendon et al*., 2014; *Ban et al*., 2015].

The AV of higher resolution simulations, for example, in regional climate models (RCMs), lies in their ability to simulate physically coherent process chains which may, or may not, modulate and improve the climate change signal [*Di Luca et al*., 2015], as has recently been demonstrated in convection-permitting simulations (CPSs) of summertime extreme subdaily precipitation [*Chan et al*., 2014b; *Kendon et al*., 2014; *Ban et al*., 2015].

Due to high computational expense, however, differences in the sensitivity of extreme precipitation to boundary forcing enhancement between parametrized and convection-permitting models, and the underlying mechanisms, have not been studied in detail, for example, over a spectrum of forcing strengths. In this respect, RCM sensitivity studies of individual extremes can be an instructive, yet inexpensive, tool. The traditional GCM or GCM-RCM approach to investigating precipitation extremes, requiring climate timescale simulations to create adequate statistics, would be hardly computationally feasible at convection-permitting resolution and over a wide range of sea surface temperature (SST) states, each representative of different climate regimes.

Downscaling to convection-permitting resolution does come with its own caveats though, as the choice of convective parametrization in the coarse domain may strongly influence the development of convection in the inner convection-permitting domain(s) [*Warner and Hsu*, 2000; *Lean et al*., 2008].

Recently, convection-permitting RCM simulations have revealed the potential for a nonlinear response of coastal extreme precipitation to SST increase [*Meredith et al*., 2015]. Here we take the devastating 2012 precipitation extreme near the Black Sea town of Krymsk as a recent showcase example and use it to explore the sensitivity of extreme precipitation to SST increase in ensemble simulations with parametrized and explicit convection, over a wide range of SST forcings. Focusing on the underlying mechanisms, we present evidence for the AV of CPSs for studying changes in convective precipitation extremes.

2. The July 2012 Krymsk Precipitation Extreme

The Krymsk precipitation extreme [*Kotlyakov et al*., 2013; *Meredith et al*., 2015] occurred on the 6/7 July 2012, along the north-eastern coast of the Black Sea. In the presence of a quasi-stationary cold upper low, a slow moving cyclone tracked across the eastern Black Sea, advecting warm and moist air toward the foothills of the Caucasus mountains (Figure 1). The precipitation affecting the Krymsk region was associated with two waves of convection, the first coming early on 6 July and the second the following night. Total precipitation of 171 mm fell in 24 h at Krymsk, a station where daily precipitation had previously not exceeded 80 mm [*Kotlyakov et al*., 2013]. The upper-level synoptic pattern that accompanied the Krymsk event fits well with the pattern, identified by *Funatsu et al*. [2009], that typically accompanies extreme summertime precipitation in the Mediterranean region [*Meredith et al*., 2015]. Additional synoptic analysis of the Krymsk event is provided in Text S1 (supporting information).

3. Methods

Changes in precipitation extremes outside of the tropics are believed to be primarily influenced by thermodynamical changes [*Emori and Brown*, 2005], rather than changes in large-scale circulation. In this framework, it is assumed that for each precipitation extreme in the present climate there is an analogous event in a future climate, occurring under a comparable atmospheric circulation but in a warmer and hence moister environment [*Lenderink and van Meijgaard*, 2008]. Working within this paradigm, we create alternate storylines [*Hazeleger et al*., 2015] of the Krymsk event for a spectrum of SST regimes and compare the sensitivity of the extreme precipitation to SST increase in simulations with parametrized and explicit convection.

3.1. Model and Experiment

The experimental setup, described in detail in *Meredith et al*. [2015], involves using the nonhydrostatic Weather Research and Forecasting (WRF) regional model [*Skamarock et al*., 2008] in a triply nested configuration (Figure 1) to simulate the Krymsk event at up to convection-permitting resolution with a range of

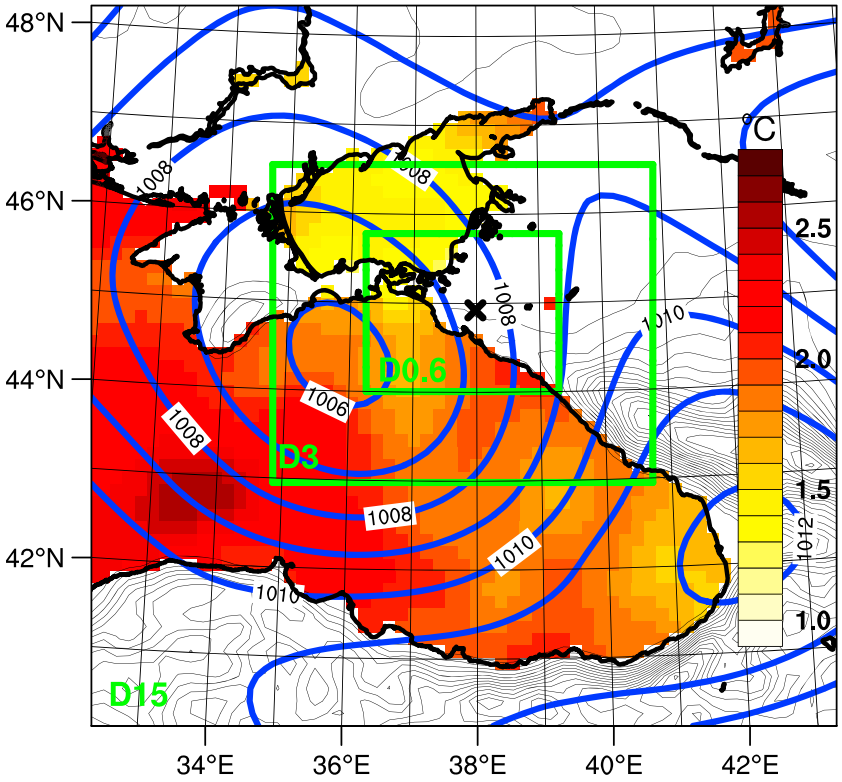

Figure 1. Sea level pressure (blue contours) on 6 July 2012 at 1800 UTC, based on NCEP Final Analyses. Simulation domains D15, D3, and D0.6 (green). The 1982–2012 SST trend across experimental domains (shading). Krymsk is marked with an "x"; light black contours denote the D15 orography field, at 150 m intervals.

Black Sea SST forcings. This is an approach often used in GCM aquaplanet simulations to emulate climate change [e.g., *Li et al.*, 2011a]. The different SST states are created by calculating the 1982–2012 trend in Black Sea SSTs (Figure 1), of a 31 day period centered on 6 July. This two-dimensional field (SST_{trend}) is then subtracted (added) from (to) the SST field observed during the event (SST_{obs}) in 20% increments. Eleven representative SST regimes are thus created, spanning 1982 (2012 minus 30) to 2042 (2012 plus 30), assuming a continuation of the SST trend. Each SST state can be described by

$$SST_i = SST_{obs} + \frac{i-5}{5} SST_{trend}, \text{ where } \quad i \in [0\,..10]. \tag{1}$$

Our method thus allows us to compare the sensitivity of extreme coastal precipitation to enhanced SSTs between simulations with parametrized and explicit convection, while keeping computational expenses relatively low.

The nesting ratio is 5:1, giving horizontal resolutions of 15, 3, and 0.6 km. Domains are referred to as D15, D3, and D0.6, respectively. Nesting is carried out on a one-way basis. Thirty-eight unevenly spaced terrain following vertical levels are used, with a model top at 10 hPa. Sensitivity tests showed the results to be insensitive to further increase in vertical resolution. Initial and lateral boundary conditions come from 1° resolution National Centers for Environmental Prediction (NCEP) Final Analyses and are updated 6-hourly. For SSTs, we use NOAA's 0.25° Optimal Interpolation data set [*Reynolds et al.*, 2007], as it is the highest resolution SST data set that is also long enough to compute climatological trends (i.e., >30 years).

We create a six-member ensemble for each SST state, using staggered initialization times, and weak spectral nudging of the U and V fields in D15 only. Nudging is carried out only above the planetary boundary layer (PBL) and at scales roughly greater than 300 km. Nudging helps to accurately maintain the large-scale circulation, without squelching the precipitation extremes [*Otte et al.*, 2012]. Additional sensitivity studies without nudging showed that the nudging we apply does not affect our conclusions but is necessary to create a larger staggered initialization time ensemble. Individual ensemble members are initialized at 6-hourly

intervals from 4 July at 00 UTC to 5 July at 06 UTC, allowing between 21 and 51 h for the atmosphere to adjust to the imposed SST forcing before the first observed precipitation of the analysis period. Tests show a convergence of the 800 hPa humidity field between all members about 9 h prior to the first wave of precipitation. Our setup gives a high signal-to-noise ratio, permitting fewer members, and allows adequate precipitation spin-up time [*Meredith et al*., 2015].

For each domain, convective processes are handled in a manner appropriate to the horizontal resolution. Convection is thus parametrized in D15, while no convective parametrization is used in D3 or D0.6. D15 thus differs from the other simulations in its horizontal resolution and in its treatment of convection. In D15, five convective parametrization schemes were tested, leading us to select the Kain-Fritsch scheme [*Kain*, 2004] (with default tuning parameters) to drive the convection-permitting domains, due to its superior simulation of the event. The extreme precipitation responses to increasing SSTs for the remaining convective parametrization schemes (D15 only), which lead to the same conclusions, are also presented.

For the analyses, we compare the D15 and D0.6 simulations over their common area, i.e., that of D0.6. Prior to analysis, all data from the fine resolution simulations are aggregated to the coarse D15 grid; this involves taking the mean of all D0.6 grid cells that are located within the area of a given D15 grid cell, for each D15 grid cell covering the D0.6 domain. As such, we compare simulations at the same spatial scales to assess the AV of CPSs, rather than simply the added small-scale detail. We attribute differences in the simulations to differences in their treatment of convection, taking account of the resolution appropriate to each method of treating convection. For extreme precipitation, we use an objective method to identify and analyze the maximum local intensity of the precipitation event, at hourly intervals. This entails considering the spatial precipitation maximum each hour, i.e., the (15 km resolution) grid cell within the D0.6 area that has the highest hourly precipitation total. We refer to this as the *hourly precipitation maximum*. Physical changes associated with the hourly precipitation maximum serve as the clearest objective illustration of changes occurring in areas of the grid affected by intense precipitation. The two waves of convection are treated separately.

4. Results

The ability of our WRF model setup to reproduce the Krymsk event with observed forcings is validated in detail, for D0.6, in *Meredith et al*. [2015]. Additional validation, provided in Appendix A, shows that the event magnitude is well captured by the D0.6 simulation. Intensities on the D0.6 native grid and their corresponding aggregation to D15 yield similar magnitudes, indicating that the highest intensities were spread over a relatively large area. D15, however, fails to fully capture the observed rainfall intensity. The compatibility of the D0.6 precipitation totals with observations gives us confidence in the faithfulness of the simulation, allowing us to treat its modeled fields as a plausible reference to compare against. Here we focus on how the event responds to boundary forcing enhancement (in our case SST) under parametrized and explicit convection.

Area average precipitation (over the common D0.6 area) during the event is qualitatively similar in the parametrized and explicit convection simulations (Figures 2a and 2b), though totals in the CPSs tend to be higher, most noticeably during the second wave of convection. The clearest difference between the two simulations is in the duration of the precipitation event. The first wave of precipitation, in particular, begins (ends) about 2 h earlier (later) with parametrized convection. Looking at hourly precipitation maxima, however, the simulations with explicit convection exhibit far higher precipitation intensities (Figures 2c and 2d), even though the results of the D0.6 simulation have been aggregated to the D15 grid. In the CPSs, maximum hourly intensities of 58–64 mm are achieved, compared to just 5–8 mm with parametrized convection. These results highlight the well-known tendency for extreme precipitation events to be too persistent, widespread, and not heavy enough in models with parametrized convection [*Kendon et al*., 2012] and point toward the AV of CPSs at local and subdaily scales. The more realistic local precipitation intensities produced by CPSs result from improved representation of convective features when convection is explicitly resolved [*Lean et al*., 2008]. In the following, we investigate these features and how their improved representation modulates the precipitation response.

Temporally averaging over each wave of convection, we can more clearly see the response shape of hourly precipitation maxima to increasing SST (Figure 3). Between the parametrized and explicit convection simulations, the transition behavior from the lowest to the highest SST notably diverges, despite the parametrized convection simulation driving the higher resolution domains. The CPSs respond overall more strongly to

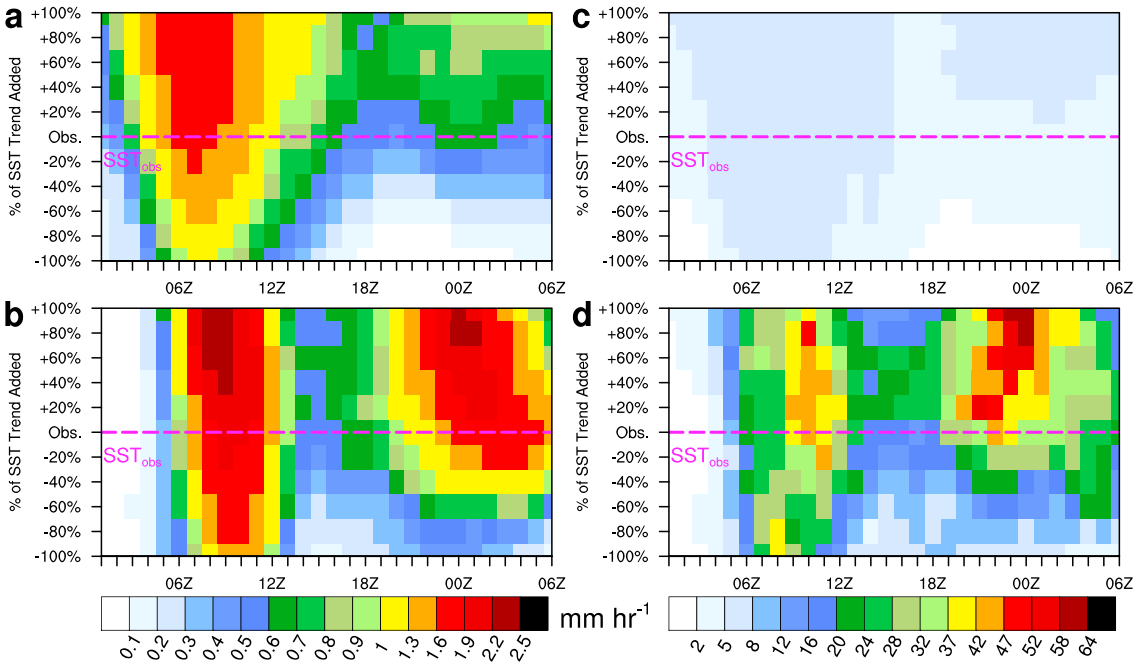

Figure 2. Temporal evolution of precipitation event for different SST forcings. Area average precipitation over inner domain area for (a) 15 km resolution simulation with parametrized convection and (b) 0.6 km resolution simulation with explicit convection. (c and d) As in Figures 2a and 2b, respectively, except for grid cell precipitation maxima. Results are based on ensemble means, all data are aggregated to the 15 km resolution grid, and only grid cells within the area of D0.6 are considered.

increasing SST, during both waves of convection. More importantly though, the CPSs exhibit a strongly nonlinear precipitation response to increasing SST, characteristic of a transition into a high-precipitation regime [*Meredith et al.*, 2015]. The nonlinear nature of the precipitation response to increasing SST is either strongly damped (first wave) or practically missed (second wave) in the simulations with parametrized convection. The nonlinear relationship also holds at the daily scale (Figure 3c). The strong divergence of the convective response in the convection-permitting D0.6 from that of the coarse D15 suggests that, in order to maximize the AV of CPSs, suitably large convection-permitting grids can be used to negate the influence of the coarse grid convective parametrization on the inner domain's solution, as speculated by *Warner and Hsu* [2000]. We use grid sizes of 156×131 and 391×321 for D3 and D0.6, respectively.

In the remainder of this section, we investigate the physical mechanisms behind the different precipitation responses. To this end, the hourly precipitation maximum provides a measure of the maximum local intensity

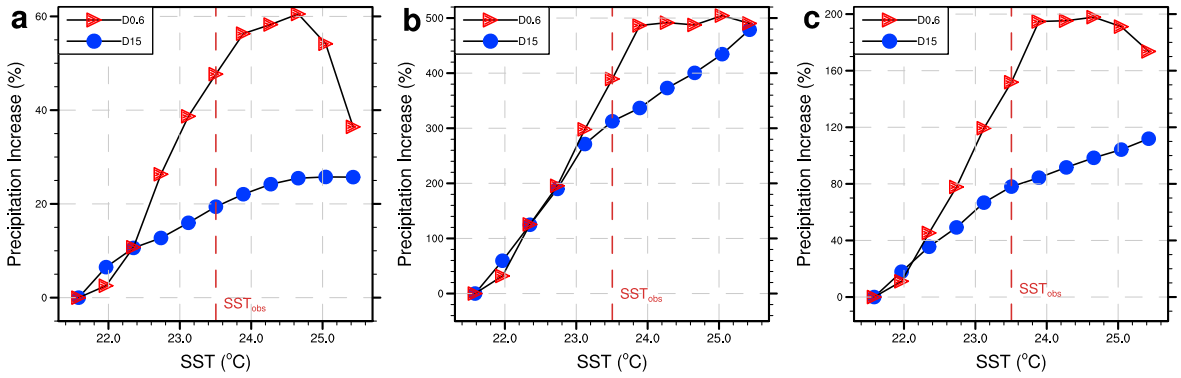

Figure 3. Extreme precipitation response to enhanced SST forcing. Increase in temporally averaged grid cell precipitation maxima during (a) the first and (b) the second waves of precipitation and (c) from the start of the first to the end of the second wave of precipitation. All data are aggregated to the 15 km resolution grid and only grid cells within the area of D0.6 are considered.

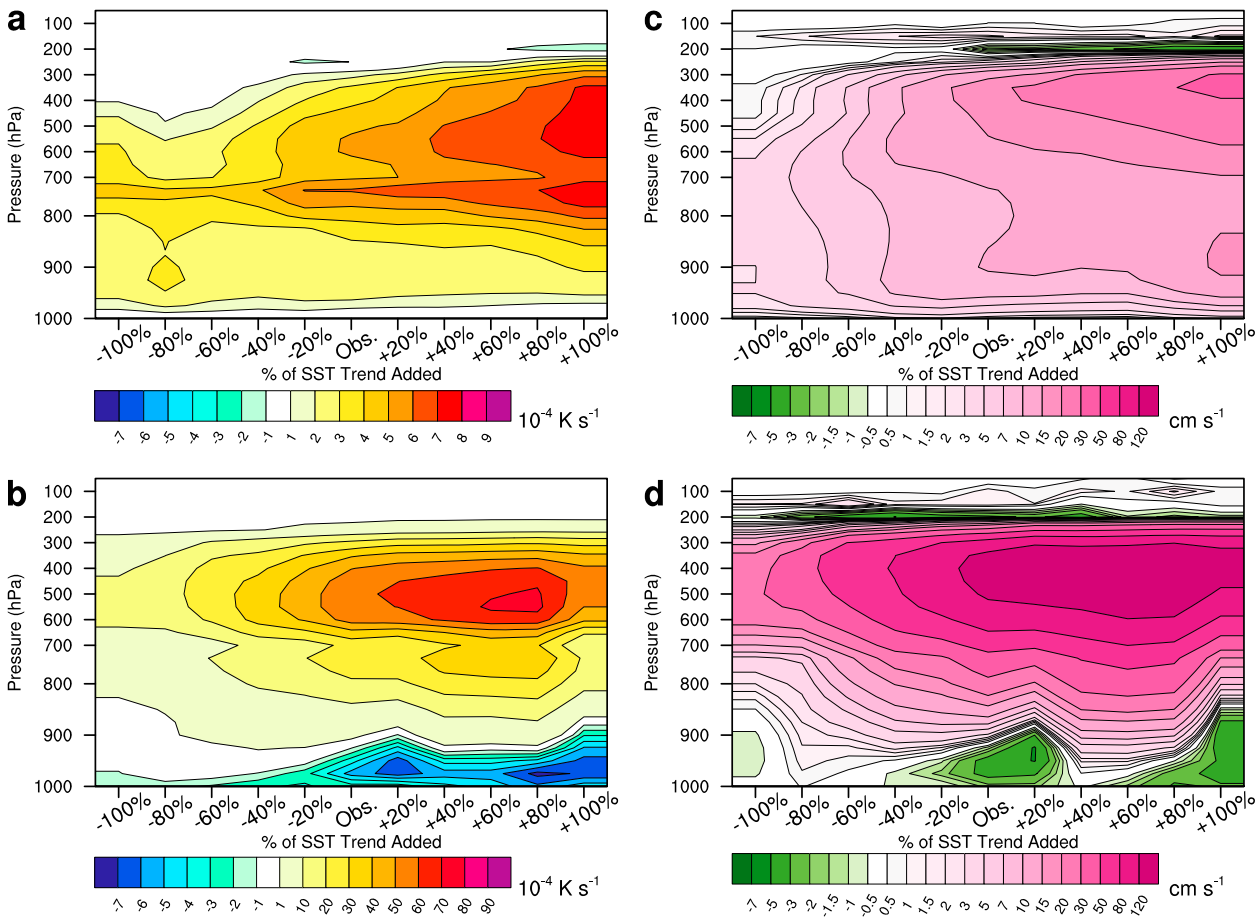

Figure 4. Impact and cause of increased precipitation intensity during the second wave of convection, for simulations with (a, c) parametrized and (b, d) explicit convection. (a, b) Latent heating response for grid cell precipitation maxima. (c, d) Vertical velocity for grid cell precipitation maxima. All data are aggregated to the 15 km resolution grid and only grid cells within the area of D0.6 are considered. A precipitation threshold of 2.0 mm hr^{-1} is used for the grid cell precipitation maxima. Latent heating is output directly by the convective parametrization (when used) and microphysics schemes. Note the different color scales between rows.

of the event and the clearest illustration of the physical effects occurring in areas affected by intense precipitation. For brevity, we focus on the second wave of convection, where the differences are more pronounced. Analysis of the first wave of convection, which leads to the same conclusions, can be found in the supporting information (Figures S4–S6).

Increasing SSTs lead to a warmer and moister lower atmosphere, increasing instability and reducing convective inhibition. To a first approximation, this should give the potential for precipitation intensity to increase in parallel. The strong differences in local precipitation intensity evident in Figure 2, however, also affect the local atmospheric profile. In particular, the more intense precipitation in the CPSs has a strong cooling effect on the PBL, which is neither evident in the parametrized convection simulations nor the colder SST states of the CPSs (Figures 4a and 4b). Such low-level cooling should act to reduce instability and increase convective inhibition in the PBL, in opposition to the effects of increased SSTs. This contributes to the flatter precipitation response seen in the CPSs once deep convection is established in the higher SST simulations. With parametrized convection, however, a net warming remains in the PBL as SSTs increase (Figure 4a).

The enhanced local precipitation intensities evident in D0.6 result from the broader distribution of vertical motions and hence vertical moisture transport that can be captured at higher resolution [*Yang et al.*, 2014]. Vigorous convection is produced on the D0.6 native grid through (resolved) locally intense updrafts (Figures 4c and 4d), which appear to be inadequately parametrized in the coarser D15 simulation. In addition to the transport of moisture and release of latent heat, updrafts also transport momentum vertically, which

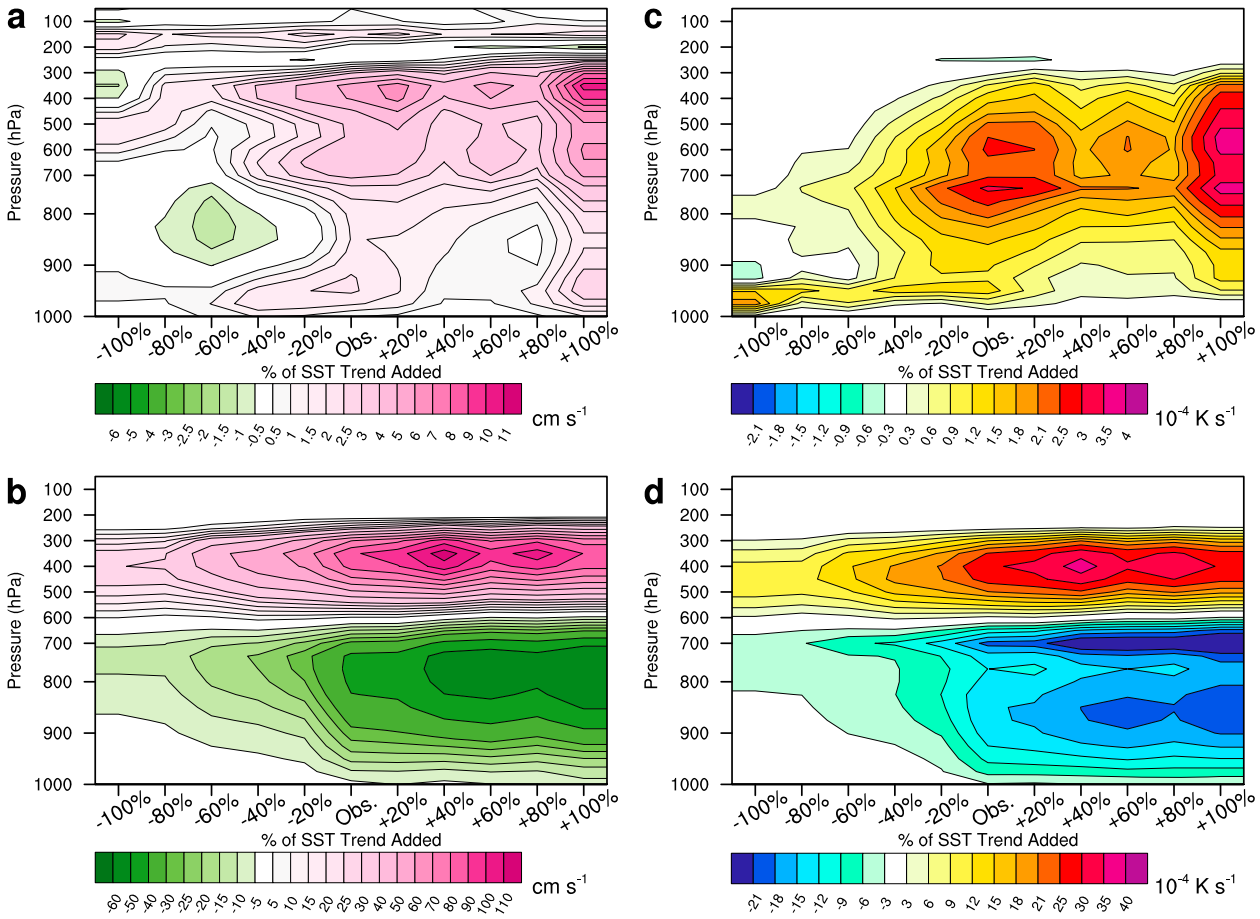

Figure 5. Impact of increased precipitation intensity during the second wave of convection, for simulations with (a, c) parametrized and (b, d) explicit convection. (a, b) Downdraft response associated with grid cell precipitation maxima, based on the maximum downdraft either in or directly adjacent to the grid cell precipitation maximum. (c, d) Latent heating for Figures 5a and 5b. All data are aggregated to the 15 km resolution grid and only grid cells within the area of D0.6 are considered. A precipitation threshold of 2.0 mm hr^{-1} is used for the grid cell precipitation maxima. Additionally, to distinguish downslope winds from convective downdrafts, a modified version of *Jiménez and Dudhia* [2012] nondimensional Laplacian operator is defined to exclude downdrafts over downward sloping land (relative to wind direction). This only impacts the results of the 15 km resolution simulation and is explained in detail in Appendix A. Note the different color scales between rows.

when intense enough can perturb the local pressure field and impact the local flow [*LeMone et al.*, 1984]. Inadequate parametrization of vertical momentum transport may thus also affect the evolution of local dynamical features within the system. The higher resolution of the D0.6 native grid also allows a more detailed representation of surface topography, which can play a key role in orographic uplift and potential subsequent convection. Additional sensitivity studies applying the D15 topography field to D0.6, however, show that in our study the more realistic surface topography in D0.6 is not a dominant factor in the triggering of deep convection or the nonlinear precipitation response.

Precipitation intensity also affects the strength of convective downdrafts. Convective downdrafts result from the evaporation of precipitation and melting of hydrometeors as they fall through the troposphere and, to a first approximation, can be thought of as scaling with precipitation intensity. Downdrafts play an influential role in convective systems. In the lower troposphere, they transport relatively low equivalent potential temperature (θ_e) air below the lifting condensation level, having a strongly stabilizing effect on the atmospheric profile [*Kain*, 2004]. If strong enough, downdrafts can also block low-level inflow [*Schoenberg Ferrier et al.*, 1996], inhibiting further convection. To analyze downdrafts associated with the hourly precipitation maxima, we consider each hour the maximum downdraft in a 3×3 neighborhood centered on the hourly precipitation maximum; this is identified based on average vertical velocities in the 1000–650 hPa layer. As SSTs increase, a strong growth in the convective downdrafts associated with the hourly precipitation maxima is only evident in the CPSs (Figures 5a and 5b). Importantly, though, it is

not just the strength of the downdrafts that increases—the depth to which downdrafts of a given strength penetrate also increases. For the coldest SST states, even the CPSs do not create strong downdrafts. Once deep convection develops in the CPSs though, the stronger downdrafts start penetrating to the surface, contributing to the flatter precipitation response. This results from increasing stability within the PBL, which can be seen by the cooling of the lower troposphere that accompanies the downdrafts in the CPSs (Figure 5d). As it is expected that the coarser simulation with parametrized convection cannot generate grid-scale vertical motions comparable to those under explicit convection, the convective parametrization scheme is intended to account for the unresolved vertical motions through environmental mass fluxes, redistributing heat and moisture throughout the column. Despite this, the parametrized convection simulations show no evidence of low-level latent cooling comparable to that when convection is explicitly resolved (Figures 5c and 5d). Area averaged convective inhibition (CIN) upstream of the coastal orography (not shown) decreases monotonically as SSTs increase in the parametrized convection simulations, allowing precipitation intensity to increase as SSTs increase. In the CPSs, however, the decrease in CIN due to increasing SSTs is first inhibited by the intensifying precipitation as SSTs increase and then stops completely for those ensembles with the highest SSTs, i.e., in those ensembles where deep convection takes hold and causes substantial low-level cooling. For the same reasons, the tendency for convective available potential energy to be increased by higher SSTs, while not prevented, is considerably inhibited in the CPSs relative to the parametrized convection simulations (not shown).

Ignoring momentum considerations, downdrafts will penetrate downward until they are either warmer than their surroundings or they reach the surface. Lower relative humidity, and hence lower cloudiness, favors the generation of stronger downdrafts [*Knupp and Cotton*, 1985] through increased evaporation of precipitation in the lower troposphere and the resultant greater latent heat of evaporation. As such, differences in the relative humidity profiles between the parametrized and explicit convection simulations can contribute to differences in the representation of downdrafts, even those aggregated to the coarser 15 km resolution. The column relative humidity profiles 1 h prior to the hourly precipitation maxima show marked differences between the simulations with parametrized and explicit convection. With parametrized convection, relative humidity is noticeably higher in the lower troposphere, as compared with the CPSs; this is in line with the tendency of CPSs to reduce the positive bias in cloud cover shown by models with parametrized convection [*Prein et al*., 2015]. Additionally, relative humidity in the parametrized convection simulations does not show the same tendency to decrease with increasing SSTs that is exhibited in the CPSs (Figure 6). This may be due to the parametrized treatment of downdrafts during the preceding integration of the model, within D15. The Kain-Fritsch scheme derives humidity profiles based on a number of microphysical assumptions, one of which is a constant rate of decrease of downdraft relative humidity with distance beneath the cloud base, which may not be suitable for extreme precipitation. As such, cloud base height can strongly influence subsequent changes in the lower troposphere relative humidity profile. Another explanation may be stronger downward motions in the CPSs, in response to enhanced vertical velocities, which would have a stronger drying effect on the atmosphere, thus reducing relative humidity and cloudiness. The decreased midtropospheric relative humidity simulated at higher SSTs, which is only evident in the CPSs, may also play an important role in inhibiting the development of secondary cells [*Shepherd et al*., 2001], contributing to the tipping point nature of the precipitation response.

The described low-level cooling in the CPSs, due to more intense precipitation and convective downdrafts, also affects the mechanisms by which subsequent convection is triggered and the location where this happens. Assuming the presence of an adequate moisture source and conditional instability, the final ingredient required for convection is uplift [e.g., *Doswell*, 1987]. In our study, a consistent source of uplift is provided by the coastal orography, which presents an abrupt barrier roughly perpendicular to the onshore flow. This is key to the high local intensities [*Kotlyakov et al*., 2013] observed during the event. As the hourly precipitation intensity increases though, the outflow associated with increasing low-level cooling extends out over the sea, behaving like a gravity current [*Corfidi*, 2003] emanating from the coastal orography. The resulting near-surface cold pools over the sea provide another source of uplift upstream of the coastal orography and result in more convection being triggered over the sea in the higher SST ensembles (Figure 7). The precipitation-cooled outflow associated with this new convection over the sea subsequently extends the outflow boundary even further from the coast. This is evident in the back building of the mesoscale convective system that is simulated at warmer SST states and found in satellite

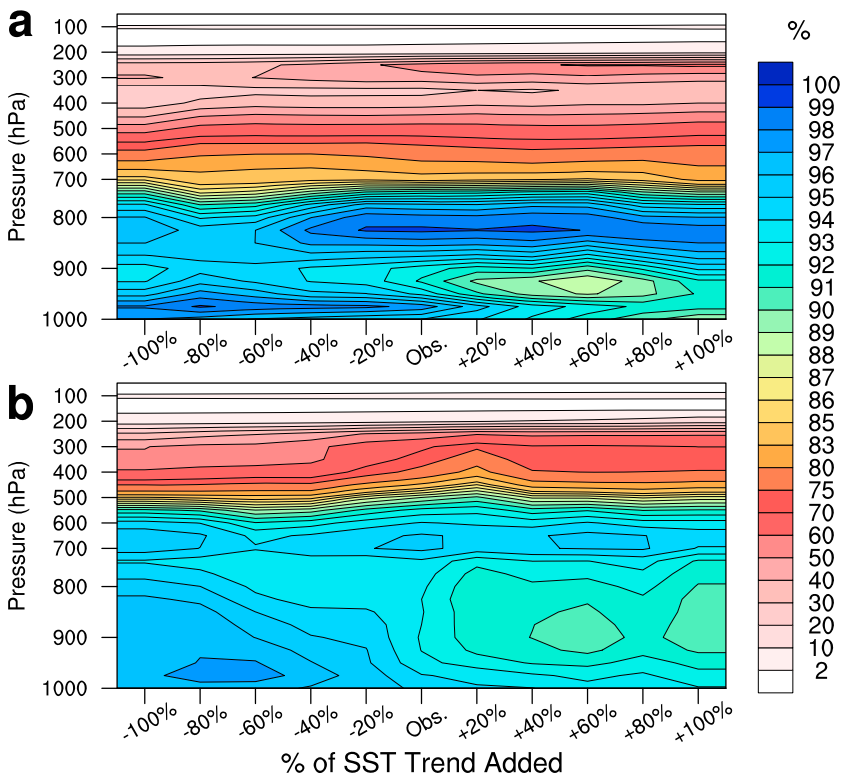

Figure 6. As in Figure 5, except for relative humidity in the maximum precipitation column 1 h prior to the downdraft. (a) D15 and (b) D0.6.

observations of the event (not shown). The near-surface cold pools over the sea also provide a smoother and less vigorous uplift than the coastal orography, potentially limiting the precipitation intensity increase. As these air parcels continue downstream toward the coastal orography, they arrive drier and more stable due to the preceding convective processes which, in turn, limits the intensity of subsequent precipitation triggered by orographic uplift. The absence of low-level cold pools in the parametrized convection simulations means that this effect is only evident in the CPSs.

The same sensitivity experiments (for D15 only) carried out with four other convective parametrization schemes (Table 1) found precipitation responses ranging from essentially flat to strongly monotonic (Figure 8), highlighting the dependence of projections of convective precipitation extremes on the choice of parametrization scheme. None of the schemes were capable of reproducing the nonlinear response shown under explicit convection. This suggests that our results demonstrate an inherent limitation of convective parametrization schemes, rather than a peculiarity of the scheme we focus on.

5. Discussion and Conclusions

Taking the 2012 Krymsk precipitation extreme as a recent showcase example, we have demonstrated over a large range of SST forcings how the response of extreme coastal precipitation to SST increase can be substantially different in CPSs than in coarser models with parametrized convection. Specifically, we have shown how the fine-scale representation of precipitation intensity and vertical motions in CPSs can strongly modulate the extreme precipitation response to SST increase at both the daily and subdaily timescale. Resolving these processes adds value by enabling key features, such as near-surface cooling and deeper penetrating downdrafts, to explicitly develop and affect the precipitation response. The tendency for reduced lower tropospheric relative humidity in the CPSs further contributes to the strong nonlinearity of the extreme precipitation response.

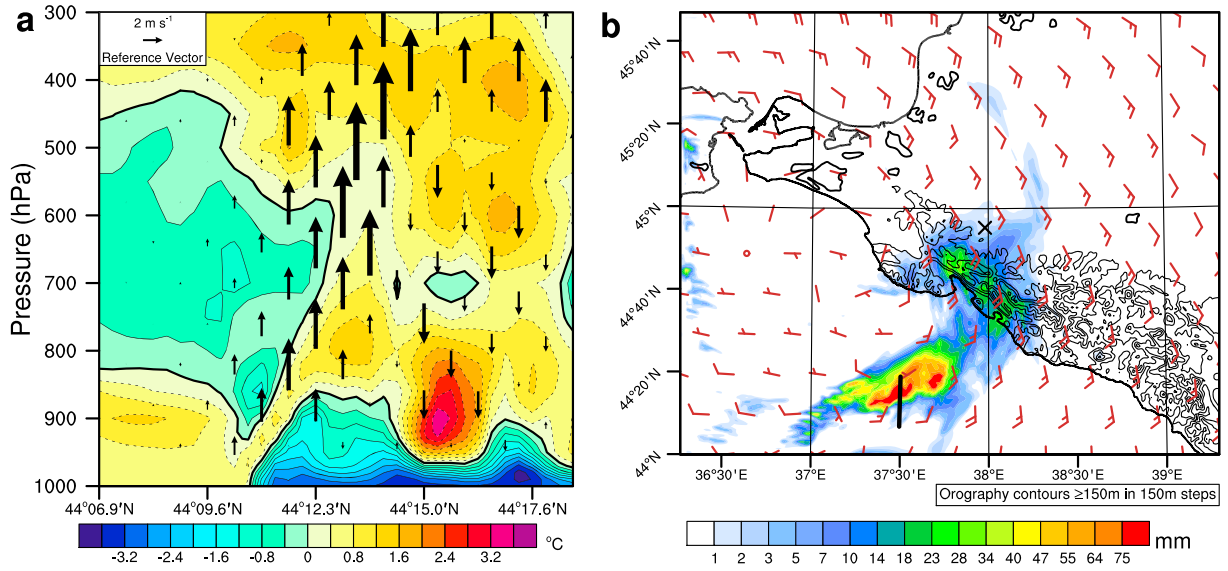

Figure 7. Cold pool triggered convection. (a) D0.6 cross section (marked in Figure 7b) showing instantaneous temperature anomaly and vertical motion for one member of the warmest SST ensemble at 0200 UTC on 7 July 2012, during the second wave of convection. The temperature anomaly is relative to the mean temperature across the west-east dimension of the grid (also at 0200 UTC), with only points over the sea considered. Convection can be seen initiating at the edge of the near-surface cold pool, before continuing in the direction of the flow (see Figure 7b). The 0°C anomaly contour is marked with a thick black line. (b) Accumulated precipitation in the hour leading up to the snapshot in Figure 7a, with the cross section along 37.5°E marked in black. Wind barbs illustrate the instantaneous flow at 850 hPa, in m s^{-1}.

In GCM aquaplanet experiments with parametrized convection and relatively coarse resolutions, *Yang et al.* [2014] identified subgrid-scale variability of vertical moisture transport (primarily due to changes in vertical velocities) as explaining most of the resolution dependence of extreme precipitation. Here we present a detailed investigation of the physical mechanisms that can also lead to a different response to SST increase of extreme precipitation in models with parametrized and explicit convection. The results highlight not only the AV of CPSs for better representing convective precipitation extremes but crucially also their AV for studying *changes* in convective extremes, which stems primarily from the increased local precipitation intensities that parametrized convection cannot reproduce. These increased intensities result from the greater spatial variability of vertical motions that the fine resolution grid can capture and play a key role in the strongly nonlinear nature of the extreme precipitation response under explicit convection, for example, by creating stronger downdrafts which transport relatively low θ_e air into the lower troposphere. The simulations with parametrized convection proved to inadequately represent the physical processes which can damp further convective intensification during extreme precipitation events.

While convective parametrization schemes can of course be tuned to better represent changes in particular extremes, a superseding requirement of climate models is for convective parametrization schemes that well represent the mean conditions across large scales, often to the detriment of regional extremes. Convective parametrization schemes which consider a much broader distribution of vertical velocities at the subgrid-scale, perhaps partly stochastically determined, may go some way toward bridging the gap with convection-permitting models and better recreating the locally intense precipitation exhibited during precipitation extremes in CPSs. As we have demonstrated, this can produce effects which strongly modify the local environment and is key to the nonlinear response.

Table 1. Parametrization Schemes Used in Figure 8

Abbreviation	Scheme	Reference(s)
TIEDTKE	Tiedtke scheme	*Tiedtke* [1989] and *Zhang et al.* [2011]
NSAS	New Simplified Arakawa-Schubert scheme	*Han and Pan* [2011]
G3-D	Grell 3D Ensemble scheme	*Grell* [1993] and *Grell and Devenyi* [2002]
BMJ	Betts-Miller-Janjic scheme	*Janjic* [1994]
KF	Kain-Fritsch scheme	*Kain* [2004]

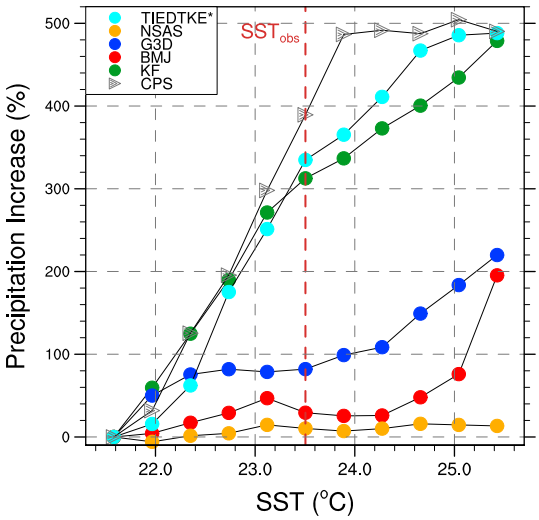

Figure 8. D15 extreme precipitation response to enhanced SST forcing with different convective parametrization schemes. Increase in temporally averaged grid cell precipitation maxima during the second wave of precipitation. For illustration, the convection-permitting simulation is also shown in gray (CPS, triangles). Note that the response of the Tiedtke scheme (cyan) has been scaled by a factor of 0.25 so that the shape of all response curves can be seen clearly in the same panel. The legend is explained in Table 1. As in Figure 3, results are based on ensemble means, all data are aggregated to the 15 km resolution grid, and only grid cells within the area of D0.6 are considered.

Eden et al. [2014] argue that it is difficult to demonstrate AV in RCMs for simulating present-day local precipitation extremes, compared to GCMs, once relatively simple statistical postprocessing [*Wong et al.*, 2014] to correct for biases and scale gaps has been applied to both simulations. For detecting the response to warming of extreme precipitation, though, bias correction methods suffer from essentially inheriting the wrong climate change trends from the climate model. As demonstrated here, CPSs are not limited in this way. Rather, the AV of CPSs is set apart from other downscaling methods by its origin in the simulation of independent, often highly localized, physical process chains.

Fine-scale processes are known to play an important role in modulating the response of daily precipitation extremes to climate change, particularly in coastal areas dominated by convective precipitation [*Diffenbaugh et al.*, 2005]. Our results raise questions about the ability of models with parametrized convection to accurately represent the response of subdaily to daily convective extremes to climatic changes in coastal regions. If the response to warming of convective extremes, particularly those in coastal regions, is of interest, then convective parametrization schemes would have to be substantially improved. Furthermore, one could conceive developing statistical postprocessing methods which include local-scale meteorological information. Absent such advances, CPSs are required not only to capture the magnitude of the response between individual states [*Kendon et al.*, 2014] but also the shape of the response across multiple states, which can be highly nonlinear.

Appendix A: Further Validation of Model Simulation, Against Observed Precipitation

The primary validation of our simulations is carried out in *Meredith et al.* [2015] (including supplementary information therein). Here we carry out additional validation of 24 h precipitation totals at Krymsk, using simulations D15 and D0.6, with the latter aggregated to the 15 km resolution grid.

To account for the simulated precipitation field potentially being (spatially) shifted from the observed field, we select the grid cell containing Krymsk and then consider all precipitation simulated within one grid cell either side of this. This gives a 3×3 box centered on Krymsk, for each ensemble member. We then create box-and-whisker plots to analyze the distribution of 24 h precipitation totals across all members and boxes. Whiskers represent the 5th and 95th percentiles, with the box representing the 25th and 75th percentiles, and the median.

Figure A1 shows box-and-whisker plots for (a) D15; (b) D0.6 aggregated to D15; (c) D0.6 on its native grid (0.6 km resolution), with a box covering the same area as the 3×3 boxes in Figures A1a and A1b; (d) D0.6 on its native grid (0.6 km resolution), except with a smaller box covering only 15 km $\times$ 15 km, i.e., equivalent to one grid cell in D15.

As can be seen in Figure A1a, the coarse resolution simulation with parametrized convection (D15) is not capable of reproducing the intense precipitation observed at Krymsk (yellow bars). Once convection is explicitly represented, however, the observed total at Krymsk fits well within the distribution of simulated 24 h precipitation totals (Figure A1b), even though the data have been aggregated to the 15 km resolution grid.

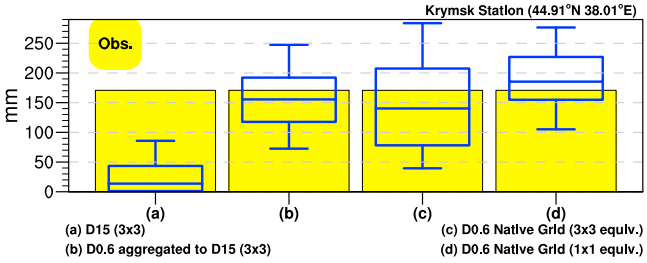

Figure A1. The 24 h precipitation observed (yellow) and simulated (box-and-whiskers) at Krymsk weather station.

This is also true of the simulated totals on the D0.6 native grid (Figures A1c and A1d). The reduced magnitude of the upper percentiles once D0.6 has been aggregated to D15, compared to those on the D0.6 native grid, illustrate the effect of aggregation on the precipitation field: the most intense localized precipitation is smoothed out. Even with this scaling effect, however, the precipitation intensities in D0.6 are still compatible with observations and are not reduced to the level of those in D15, further suggesting that the results of the D15 experiment stem from the inadequate parametrization of convective processes associated with extreme precipitation.

While these results are good, it is important to add the caveat that there is a considerable degree of spatial randomness inherent in precipitation totals recorded at point locations, i.e., at the Krymsk weather station. As such, one cannot necessarily expect point totals to be representative of the broader precipitation field.

Appendix B: Further Information on the Measurement of Downdrafts From the Model Output

As demonstrated in the main text, vertical motions due to convective activity are much smaller in D15 than in D0.6. As a result, the strongest downward motions simulated in D15 actually result from downslope winds, rather than convective downdrafts. To create Figure 5 in the main text, we need to be able to distinguish between downslope winds and convective downdrafts.

This is achieved, first, by each time step only considering downdrafts either in or directly adjacent to the maximum precipitation cell (i.e., a 3×3 box on the D15 grid, centered on the maximum precipitation cell). Second, we define a modified version of *Jiménez and Dudhia* [2012] nondimensional Laplacian operator, to also exclude grid cells with downward slopes (relative to the wind direction) over a certain threshold from consideration. The maximum downdraft is then determined as described in the main text, using the remaining nonexcluded grid cells in the 3×3 box.

To distinguish topographic features in a regional model, *Jiménez and Dudhia* [2012] apply the following operator to the topographic field h:

$$\Delta^2 h_{i,j} = 0.25\left(h_{i+1,j} + h_{i,j+1} + h_{i-1,j} + h_{i,j-1} - 4h_{i,j}\right) \tag{B1}$$

which they term the nondimensional Laplacian operator and is related to the traditional Laplacian operator by $\nabla^2 h = \Delta^2 h/(\Delta x)^2$.

We modify equation (B1) to take account of wind direction, giving four different operators, to be used according to which quadrant (i.e., NE, SE, SW, and NW) the wind direction vector is located in.

$$\text{NE}: \Delta^2 h_{i,j} = A^{-1}\left(h_{i,j+1} + h_{i+1,j} + \frac{1}{\sqrt{2}} h_{i+1,j+1} - A h_{i,j}\right) \tag{B2}$$

$$\text{SE}: \Delta^2 h_{i,j} = A^{-1}\left(h_{i,j-1} + h_{i+1,j} + \frac{1}{\sqrt{2}} h_{i+1,j-1} - A h_{i,j}\right) \tag{B3}$$

$$\text{SW}: \Delta^2 h_{i,j} = A^{-1}\left(h_{i,j-1} + h_{i-1,j} + \frac{1}{\sqrt{2}} h_{i-1,j-1} - A h_{i,j}\right) \tag{B4}$$

$$\text{NW}: \Delta^2 h_{i,j} = A^{-1}\left(h_{i,j+1} + h_{i-1,j} + \frac{1}{\sqrt{2}} h_{i-1,j+1} - A h_{i,j}\right), \tag{B5}$$

where $A = \frac{1+2\sqrt{2}}{\sqrt{2}}$. Ten meter surface winds are used to determine the wind direction. Thus, for a north-east*ward* wind, negative values of equation (B2) would imply a downslope wind, with a similar argument applying to downslope winds in the remaining quadrants.

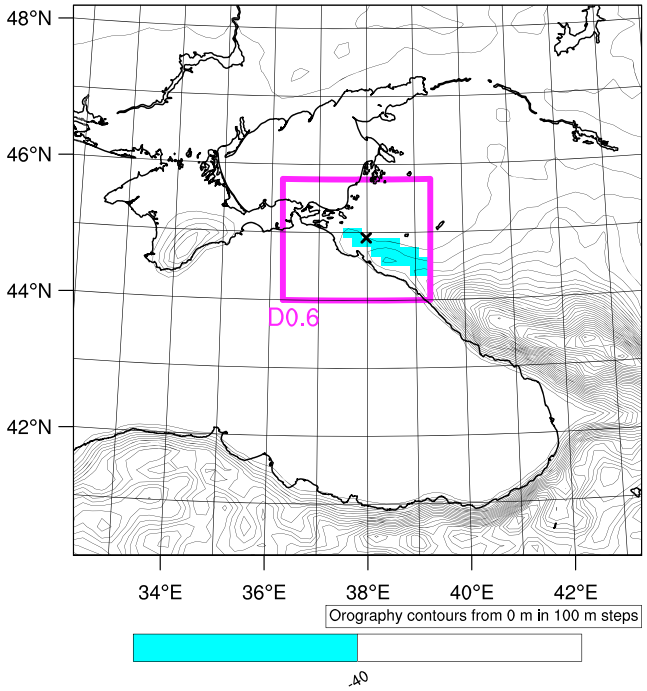

Figure B1. For a wind direction orientated in the north-eastern quadrant, the grid cells marked in blue would be excluded from consideration for calculating Figure 5.

To exclude downslope winds from our calculation of downdrafts, we set a threshold slope value of −40 for equations (B2)–(B5). Thus, for a wind direction oriented toward a given quadrant, if the corresponding modified nondimensional Laplacian operator gives a value less than −40, then the grid point is not considered for calculation of convective downdrafts.

These considerations only impact the results in D15, as the downdrafts in D0.6 are far stronger than downslope winds within that domain. If we were to simply look at downdrafts from D15, without the aforementioned specifications, the results show an almost constant "downdraft" magnitude across SST states, though decreasing slightly as higher SSTs warm the lower troposphere, giving weaker downslope winds (not shown). Figure B1 shows the grid points which would be excluded from consideration for a wind orientated within the north-eastern quadrant (the most common orientation during the event).

Acknowledgments
The authors thank A. Di Luca and two anonymous reviewers for their excellent comments which greatly improved the manuscript. NCEP Final Analyses are available online from the National Center for Environmental Prediction, at 10.5065/D6WD3XH5. Optimal Interpolation SSTs are available online from NOAA at http://www.ncdc.noaa.gov/oisst. Simulation data are available on request from the corresponding author. This study was funded by the EUREX project of the Helmholtz Association (HRJRG-308) and partially supported by the Russian Ministry of Education and Science (contract 14.B25.31.0026) and Russian Foundation for Basic Research (grant 14-05-00518). Simulations were carried out at the North-German Supercomputing Alliance (HLRN). All figures were created using the NCAR Command Language (Version 6.3.0) 10.5065/D6WD3XH5.

References

Allen, M. R., and W. J. Ingram (2002), Constraints on future changes in climate and the hydrologic cycle, *Nature*, *419*, 224–232.
Ban, N., J. Schmidli, and C. Schär (2014), Evaluation of the convection-resolving regional climate modeling approach in decade-long simulations, *J. Geophys. Res. Atmos.*, *119*, 7889–7907, doi:10.1002/2014GL062588.
Ban, N., J. Schmidli, and C. Schär (2015), Heavy precipitation in a changing climate: Does short-term summer precipitation increase faster?, *Geophys. Res. Lett.*, *42*, 1165–1172, doi:10.1002/2014JD021478.
Chan, S. C., E. J. Kendon, H. J. Fowler, S. Blenkinsop, N. M. Roberts, and C. A. T. Ferro (2014a), The value of high-resolution Met Office regional climate models in the simulation of multihourly precipitation extremes, *J. Clim.*, *27*, 6155–6174.
Chan, S. C., E. J. Kendon, H. J. Fowler, S. Blenkinsop, and N. M. Roberts (2014b), Projected increase in summer and winter UK sub-daily precipitation extremes from high-resolution regional climate models, *Clim. Dyn.*, *41*, 1475–1495.
Corfidi, S. F. (2003), Cold pools and MCS propagation: Forecasting the motion of downwind-developing MCSs, *Weather Forecasting*, *18*(6), 997–1017.
Di Luca, A., R. de Elía, and R. Laprise (2012), Potential for added value in precipitation simulated by high-resolution nested regional climate models and observations, *Clim. Dyn.*, *38*(5-6), 1229–1247.
Di Luca, A., R. de Elía, and L. René (2015), Challenges in the quest for added value of regional climate dynamical downscaling, *Curr. Clim. Change Rep.*, *1*(1), 10–21.
Diffenbaugh, N. S., J. S. Pal, R. J. Trapp, and F. Giorgi (2005), Fine-scale processes regulate the response of extreme events to global climate change, *Proc. Natl. Acad. Sci. U.S.A.*, *102*(44), 15,774–15,778.
Donat, M. G., et al. (2013), Updated analyses of temperature and precipitation extreme indices since the beginning of the twentieth century: The HadEX2 data-set, *J. Geophys. Res. Atmos.*, *118*, 2098–2118, doi:10.1002/jgrd.50150.
Doswell, C. A., III (1987), The distinction between large-scale and mesoscale contribution to severe convection: A case study example, *Weather Forecasting*, *2*(1), 3–16.
Eden, J. M., M. Widmann, D. Maraun, and M. Vrac (2014), Comparison of GCM- and RCM-simulated precipitation following stochastic postprocessing, *J. Geophys. Res. Atmos.*, *119*, 11,040–11,053, doi:10.1002/2014JD021732.
Emori, S., and S. J. Brown (2005), Dynamic and thermodynamic changes in mean and extreme precipitation under changed climate, *Geophys. Res. Lett.*, *32* L17706, doi:10.1029/2005GL023272.
Feser, F., B. Rockel, H. von Storch, J. Winterfeldt, and M. Zahn (2011), Regional climate models add value to global model data: A review and selected examples, *Bull. Am. Meteorol. Soc.*, *92*(9), 1181–1192.
Funatsu, B. M., C. Claud, and J.-P. Chaboureau (2009), Comparison between the large-scale environments of moderate and intense precipitating systems in the Mediterranean region, *Mon. Weather Rev.*, *137*, 3933–3959.
Grell, G. A. (1993), Prognostic evaluation of assumptions used by cumulus parameterizations, *Mon. Weather Rev.*, *121*, 764–787.
Grell, G. A. and D. Devenyi (2002), A generalized approach to parameterizing convection combining ensemble and data assimilation techniques. *Geophys. Res. Lett.*, *29*(14), 1693, doi:10.1029/2002GL015311.
Groisman, P. Y., R. W. Knight, D. R. Easterling, T. R. Karl, G. C. Hegerl, and V. N. Razuvaev (2005), Trends in intense precipitation in the climate record, *J. Clim.*, *18*, 1326–1350.

Han, J., and H. L. Pan (2011), Revision of convection and vertical diffusion schemes in the NCEP global forecast system, *Weather Forecasting*, *26*, 520–533.
Hazeleger, W., B. J. J. M. van den Hurk, E. Min, G. J. van Oldenborgh, A. C. Petersen, D. A. Stainforth, E. Vasileiadou, and L. A. Smith (2015), Tales of future weather, *Nat. Clim. Change*, *5*(2), 107–113.
Hohenegger, C., P. Brockhaus, and C. Schär (2008), Towards climate simulations at cloud-resolving scales, *Meteorol. Z.*, *17*(4), 383–394.
Janjic, Z. I. (1994), The step–mountain eta coordinate model: Further developments of the convection, viscous sublayer, and turbulence closure schemes, *Mon. Weather Rev.*, *122*, 927–945.
Jiménez, P. A., and J. Dudhia (2012), Improving the representation of resolved and unresolved topographic effects on surface wind in the WRF model, *J. Appl. Meteorol. Climatol.*, *51*, 300–316.
Kain, J. S. (2004), The Kain–Fritsch convective parameterization: An update, *J. Appl. Meteorol.*, *43*, 170–181.
Karl, T. R., and R. W. Knight (1998), Secular trends of precipitation amount, frequency, and intensity in the United States, *Bull. Am. Meteorol. Soc.*, *79*, 231–241.
Kendon, E. J., N. M. Roberts, C. A. Senior, and M. J. Roberts (2012), Realism of rainfall in a very high resolution regional climate model, *J. Clim.*, *25*, 5791–5806.
Kendon, E., N. M. Roberts, H. J. Fowler, M. J. Roberts, S. C. Chan, and C. A. Senior (2014), Heavier summer downpours with climate change revealed by weather forecast resolution model, *Nat. Clim. Change*, *4*, 570–576.
Kharin, V., F. W. Zwiers, X. Zhang, and G. C. Hegerl (2007), Changes in temperature and precipitation extremes in the IPCC ensemble of global coupled model simulations, *J. Clim.*, *20*(8), 1419–1444.
Kitoh, A., T. Ose, K. Kurihara, S. Kusunoki, M. Sugi, and KAKUSHIN Team-3 Modeling Group (2009), Projection of changes in future weather extremes using super-high-resolution global and regional atmospheric models in the KAKUSHIN Program: Results of preliminary experiments, *Hydrol. Res. Lett.*, *3*, 49–53.
Knupp, K. R., and W. R. Cotton (1985), Convective cloud downdraft structure: An interpretive survey, *Rev. Geophys.*, *23*(2), 183–215.
Kotlyakov, V. M., L. V. Desinov, S. V. Dolgov, N. I. Koronkevich, E. A. Likhacheva, A. N. Makkaveev, A. A. Medvedev, and V. A. Rudakov (2013), Flooding of July 6–7, 2012, in the town of Krymsk, *Reg. Res. Russia*, *3*(1), 32–39, doi:10.1134/S2079970513010061.
Lean, H. W., P. A. Clark, M. Dixon, N. M. Roberts, A. Fitch, R. Forbes, and C. Halliwell (2008), Characteristics of high-resolution versions of the Met Office Unified Model for forecasting convection over the United Kingdom, *Mon. Weather Rev.*, *136*(9), 3408–3424.
LeMone, M. A., G. M. Barnes, and E. J. Zipser (1984), Momentum flux by lines of cumulonimbus over the tropical oceans, *J. Atmos. Sci.*, *41*(12), 1914–1932.
Lenderink, G., and E. van Meijgaard (2008), Increase in hourly precipitation extremes beyond expectations from temperature changes, *Nat. Geosci.*, *1*, 511–514.
Li, F., W. D. Collins, M. F. Wehner, D. L. Williamson, and J. G. Olson (2011a), Response of precipitation extremes to idealized global warming in an aqua-planet climate model: Towards a robust projection across different horizontal resolutions, *Tellus A*, *63*(5), 876–883.
Li, F., W. D. Collins, M. F. Wehner, D. L. Williamson, J. G. Olson, and C. Algieri (2011b), Impact of horizontal resolution on simulation of precipitation extremes in an aqua-planet version of Community Atmospheric Model (CAM3), *Tellus A*, *63*(5), 884–892.
Meredith, E. P., V. A. Semenov, D. Maraun, W. Park, and A. V. Chernokulsky (2015), Crucial role of Black Sea warming in amplifying the 2012 Krymsk precipitation extreme, *Nat. Geosci.*, *8*, 615–619.
Orlowsky, B., and S. I. Seneviratne (2011), Global changes in extreme events: Regional and seasonal dimension, *Clim. Change*, *110*, 669–696.
Otte, T. L., C. G. Nolte, M. J. Otte, and J. H. Bowden (2012), Does nudging squelch the extremes in regional climate modeling?, *J. Clim.*, *25*(20), 7046–7066.
Prein, A. F., A. Gobiet, M. Suklitsch, H. Truhetz, N. K. Awan, K. Keuler, and G. Georgievski (2013), Added value of convection permitting seasonal simulations, *Clim. Dyn.*, *41*(9-10), 2655–2677.
Prein, A. F., et al. (2015), A review on regional convection-permitting climate modeling: Demonstrations, prospects, and challenges, *Rev. Geophys.*, *53*, 323–361, doi:10.1002/2014RG000475.
Reynolds, R. W., T. M. Smith, C. Liu, D. B. Chelton, K. S. Casey, and M. G. Schlax (2007), Daily high resolution blended analyses for sea surface temperature, *J. Clim.*, *20*, 5473–5496.
Schoenberg Ferrier, B., J. Simpson, and W.-K. Tao (1996), Factors responsible for precipitation efficiencies in midlatitude and tropical squall simulations, *Mon. Weather Rev.*, *124*(10), 2100–2125.
Semenov, V. A., and L. Bengtsson (2002), Secular trends in daily precipitation characteristics: Greenhouse gas simulation with a coupled AOGCM, *Clim. Dyn.*, *19*, 123–140.
Seneviratne, S. I., et al. (2012), Changes in climate extremes and their impacts on the natural physical environment, in *Managing the Risks of Extreme Events and Disasters to Advance Climate Change Adaptation*, *A Spec. Rep. of Working Groups I and II of the Intergovernmental Panel on Clim. Change (IPCC)*, edited by C. B. Field, pp. 109–230, Cambridge Univ. Press, Cambridge, U. K., and New York.
Shepherd, J. M., B. S. Ferrier, and P. S. Ray (2001), Rainfall morphology in Florida convergence zones: A numerical study, *Mon. Weather Rev.*, *129*(2), 177–197.
Skamarock, W. C., J. B. Klemp, J. Dudhia, D. O. Gill, D. M. Barker, M. G. Duda, X.-Y. Huang, W. Wang, and J. G. Powers (2008), A description of the advanced research WRF version 3 NCAR Tech. Note NCAR/TN-475 + STR, 125 pp.
Tiedtke, M. (1989), A comprehensive mass flux scheme for cumulus parameterization in large–scale models, *Mon. Weather Rev.*, *117*, 1779–1800.
Trenberth, K. E. (1999), Conceptual framework for changes of extremes of the hydrological cycle with climate change, in *Weather and Climate Extremes*, pp. 327–339, Springer, Netherlands.
Volosciuk, C., D. Maraun, V. A. Semenov, and W. Park (2015), Extreme precipitation in an atmosphere general circulation model: Impact of horizontal and vertical model resolution, *J. Clim.*, *28*(3), 1184–1205.
Warner, T. T., and H.-M. Hsu (2000), Nested-model simulation of moist convection: The impact of coarse-grid parameterized convection on fine-grid resolved convection, *Mon. Weather Rev.*, *128*(7), 2211–2231.
Wong, G., D. Maraun, M. Vrac, M. Widmann, J. M. Eden, and T. Kent (2014), Stochastic model output statistics for bias correcting and downscaling precipitation including extremes, *J. Clim.*, *27*(18), 6940–6959.
Yang, Q., L. R. Leung, S. A. Rauscher, T. D. Ringler, and M. A. Taylor (2014), Atmospheric moisture budget and spatial resolution dependence of precipitation extremes in aquaplanet simulations, *J. Clim.*, *27*(10), 3565–3581.
Zhang, C., Y. Wang, and K. Hamilton (2011), Improved representation of boundary layer clouds over the Southeast Pacific in ARW–WRF using a modified Tiedtke cumulus parameterization scheme, *Mon. Weather Rev.*, *139*, 3489–3513.